



Printability during projection-based 3D bioprinting

Kang Yu^{a,1}, Xinjie Zhang^{b,e,1}, Yuan Sun^{a,d}, Qing Gao^{a,d}, Jianzhong Fu^{a,d}, Xiujun Cai^{b,e}, Yong He^{a,c,f,*}

^a State Key Laboratory of Fluid Power and Mechatronic Systems, College of Mechanical Engineering, Zhejiang University, Hangzhou 310027, China

^b Department of General Surgery, Sir Run-Run Shaw Hospital, Zhejiang University School of Medicine, Hangzhou 310016, China

^c Key Laboratory of Materials Processing and Mold, Zhengzhou University, Zhengzhou, 450002, China

^d Key Laboratory of 3D Printing Process and Equipment of Zhejiang Province, College of Mechanical Engineering, Zhejiang University, Hangzhou 310027, China

^e Zhejiang Research and Development Engineering Laboratory of Minimally Invasive Technology and Equipment, Hangzhou, 310016, China

^f Cancer Center, Zhejiang University, Hangzhou, Zhejiang 310058 China

ARTICLE INFO

Keywords:

Projection-based printing (PBP)
3D bioprinting
GelMA bioink
Rheological analysis

ABSTRACT

Since projection-based 3D bioprinting (PBP) could provide high resolution, it is well suited for printing delicate structures for tissue regeneration. However, the low crosslinking density and low photo-crosslinking rate of photocurable bioink make it difficult to print fine structures. Currently, an in-depth understanding of the is lacking. Here, a research framework is established for the analysis of printability during PBP. The gelatin methacryloyl (GelMA)-based bioink is used as an example, and the printability is systematically investigated. We analyze the photo-crosslinking reactions during the PBP process and summarize the specific requirements of bioinks for PBP. Two standard quantized models are established to evaluate 2D and 3D printing errors. Finally, the better strategies for bioprinting five typical structures, including solid organs, vascular structures, nerve conduits, thin-wall scaffolds, and micro needles, are presented.

1. Introduction

As a powerful cell assembly technology, 3-dimensional (3D) bioprinting has been widely used in tissue repair [1–3], disease model establishment [4–6], drug screening [7–10], clinical treatments [11–15], and other applications. In recent years, vat photopolymerization (VP) [50,51], including stereo lithography (SLA), projection-based printing, two-photon polymerization (TPP), and other printing technologies has shown significant potential in bio-manufacturing. PBP, a VP method, has attracted increasing attention in biomedical fields due to its high resolution and rapid printing speed [16–18]. Complex structures can be fabricated rapidly using PBP, significantly increasing the printing precision and complexity of the printed products. Bioinks have excellent bio-performance in an aqueous environment, enabling the creation of a 3D cell environment [19–21]. However, due to their high water content and low crosslinking density, the manufacturing and operating process are complicated. Thus, it is necessary to reach a balance between bio-performance and operability

during PBP.

Printability refers to the printing accuracy and standardization of the printing process, including the material selection and parameter configuration. After years of investigation, the printability research of extrusion-based bioprinting (EBP) is relatively mature [21–25], whereas the printing behavior during PBP has rarely been addressed. The selection of the bioink is the first step in printability research. Unlike EBP, PBP has unique requirements for printing materials to match the photo-crosslinking process. In addition to good fluidity, the bioinks used in PBP also require excellent photo-crosslinking properties to ensure fast curing and high fidelity. Once the composition of the bioink has been determined, the optimum parameters are defined within a certain range. In practical applications, the bioink composition should be adjustable according to the biomedical requirements, i.e., platelet-rich plasma (PRP) [26,27], drugs [28,29], and cells [30–34]. Therefore, it is difficult to develop a unified parameter window for printing. The printing quality is improved when a suitable printing window is configured.

Here, we propose an experimental method to investigate the

Peer review under responsibility of KeAi Communications Co., Ltd.

* Corresponding author. State Key Laboratory of Fluid Power and Mechatronic Systems, College of Mechanical Engineering, Zhejiang University, Hangzhou 310027, China.

E-mail address: yongqin@zju.edu.cn (Y. He).

¹ These authors contributed equally to this work.

<https://doi.org/10.1016/j.bioactmat.2021.09.021>

Received 1 July 2021; Received in revised form 27 August 2021; Accepted 14 September 2021

Available online 21 September 2021

2452-199X/© 2021 The Authors. Publishing services by Elsevier B.V. on behalf of KeAi Communications Co. Ltd. This is an open access article under the CC

BY-NC-ND license (<http://creativecommons.org/licenses/by-nc-nd/4.0/>).

printability of PBP using GelMA hydrogel as the base component of the bioink to configure the printing materials and adjust the parameters to achieve high-quality results. The framework of the printability analysis is divided into four parts, as shown in Fig. 1. First, the PBP printing process is analyzed, and the three requirements of the materials are determined as guidance for material selection. Next, the photo-crosslinking mechanism of GelMA is analyzed to understand the curing process. For the bioink assessment, we propose the use of the indices $\Delta G'$ (the difference in the storage modulus G' between the crosslinked and non-crosslinked states on the log scale) and ΔM (the difference between the storage modulus G' and loss modulus G'') derived from the rheological analysis to evaluate the printing performance and determine the optimum PBP printing parameters. Subsequently, the photo-crosslinking process during PBP is investigated to determine the effect of the printing parameters. The two-dimensional (2D) and 3D printing errors are analyzed systematically for parameter optimization. “Spokes” and “Winding stairs” models are proposed to evaluate the printing errors quantitatively. Five printing strategies are proposed for five typical structures used in clinical biomedical applications, providing guidance for model design and printing parameter selection using bioinks.

2. Mechanism of projection-based 3D bioprinting

The printing system of PBP is composed of three parts: the platform, ink tank, and projector, as shown in Fig. 2A. The designed digital models are sliced into layers by the printing software before printing. During the printing, the platform is submerged into the ink tank to a distance of a one-layer thickness from the bottom of the tank. The ink tank is filled

with photocurable bioink, and the bottom of the ink tank consists of a transparent film that is light and oxygen permeable. The model slices are imported into the digital micro-mirror device (DMD) chip, and the emitted light is reflected by the DMD chip. A pattern is projected onto the bottom of the ink tank, and the bioink exposed to light is crosslinked, whereas the unexposed bioink remains liquid. Then the platform moves up by a distance of one layer to create the next layer. The process is repeated layer-by-layer to fabricate the 3D structure.

The manufacturing process consists of repeated printing of single layers. Thus, it is important to assess what occurs during a one-layer printing loop. As shown in Fig. 2B, we find that three key steps occur during the one-layer printing loop. **Step 1:** the platform is in position, the light pattern is projected onto the bottom of the ink tank, and the bioink is crosslinked under light in seconds. **Step 2:** the printed structure retains its shape after the exposure stops. **Step 3:** the platform moves up with the attached printed structure, and the uncured bioink fills the gaps smoothly and instantaneously.

3. Bioink analysis

Due to the subsequent biomedical applications, biocompatibility and functionality of bioink should be considered in the first step. Hydrogel-based bioink has excellent bio-performance. However, it is a brand-new material used in PBP. Therefore, it is necessary to investigate the photo-crosslinking mechanism of bioink before analyzing the printability. Furthermore, the control method of the photo-crosslinking reactions during PBP should be established to evaluate the performance of 3D bioprinting.

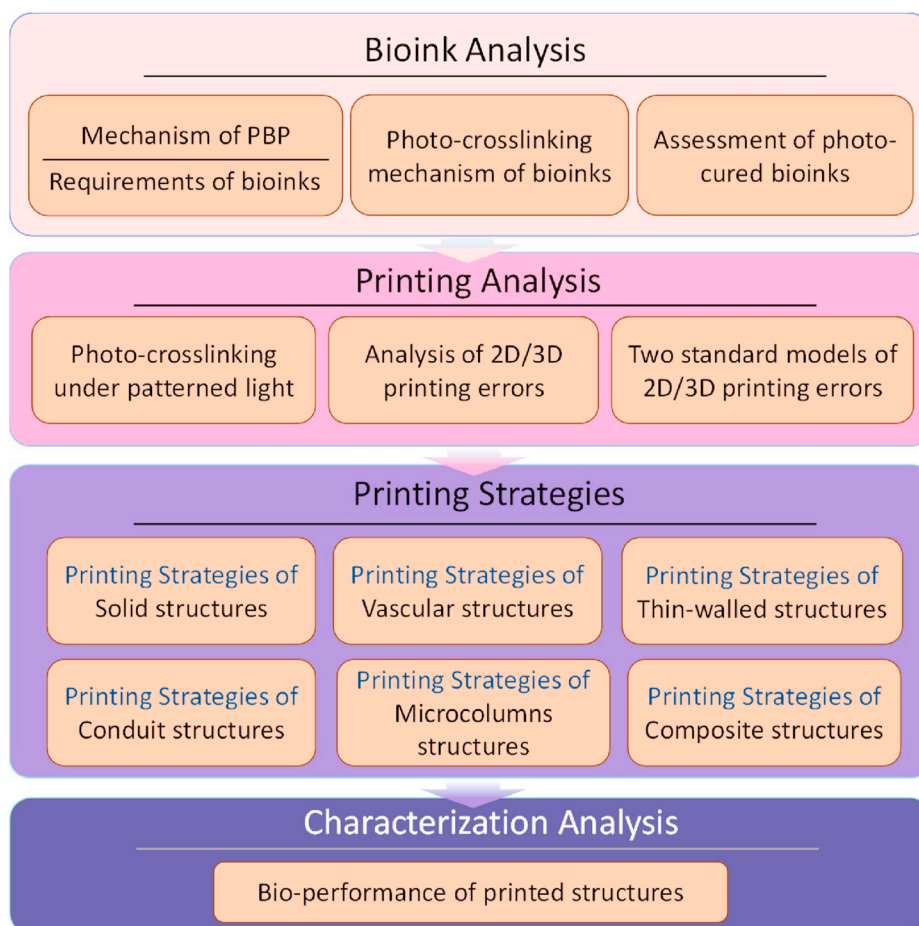


Fig. 1. The framework for analyzing the printability during projection-based 3D bioprinting (PBP).

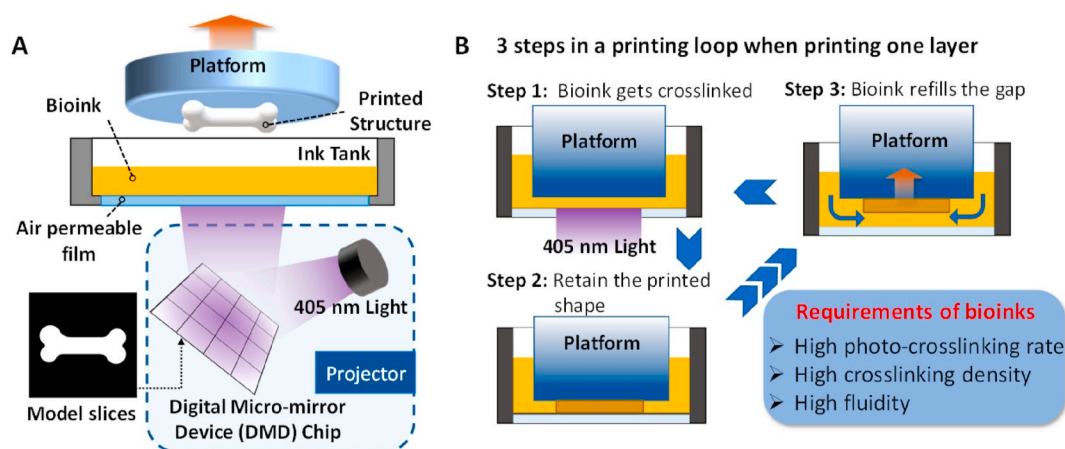


Fig. 2. The manufacturing mechanism of PBP. A) schematic diagram of the PBP system; B) three steps in a single loop during PBP and the three requirements of bioinks derived from the one-layer printing process.

3.1. Requirements of bioinks

As described in Section 2, the **requirements** of an ideal photocurable bioink are i) a **high photo-crosslinking rate**, ii) a **high crosslinking density**, and iii) **high fluidity** (Fig. 2B). In Step 1, the bioink requires a high crosslinking rate to achieve rapid curing (ideally in a few seconds) to reduce the printing time. During Step 2, it is necessary to maintain a high crosslinking density to obtain a good stiffness. In Step 3, high fluidity of the bioink is crucial to improve the printing efficiency and ensure that the uncured hydrogel bioinks can flow into the gaps and fill the spaces rapidly.

3.2. Photo-crosslinking mechanism of photocurable bioinks

The analysis of the photo-crosslinking mechanism of bioinks is the first step to optimize the printing accuracy of PBP. In this study, the bioink consists of a photocurable hydrogel (GelMA), a photoinitiator (lithium phenyl-2,4,6-trimethylbenzoylphosphine, LAP), and a light absorber (tartrazine). Since this is a free radical photosensitive material system, the photo-crosslinking process of GelMA bioink can be divided into two reactions: (1) photophysical reaction and (2) chemical crosslinking reaction [35,36]. These two reactions occur simultaneously.

In the **photophysical reaction**, the photoinitiator LAP is excited from the ground state (LAP) to the excited state (free radical) when exposed to 405 nm light [37], as shown in Fig. 3. The production rate and the number of free radicals is controlled by the light intensity and exposure time, respectively. Simultaneously, in the **chemical crosslinking reaction**, the free radicals attack the C=C double bonds on the

GelMA molecule, bonding with one of the double bonds and leaving an unbonded electron. The molecular weight of GelMA increases when it meets another unbonded electron, forming a new bond. The GelMA molecules are crosslinked into the hydrogel state.

3.3. Control of the photo-crosslinking reactions

It is crucial to control the photo-crosslinking reactions during PBP, which is achieved using a univariate method. As shown in Fig. 3, the amount of GelMA is sufficient in the chemical crosslinking reaction, and the crosslinking rate and the crosslinking density of the GelMA network depend on the production rate and the number of free radicals. Since free radicals only exist in areas where the light can penetrate due to the short half-life of free radicals [38], the production rate and density of crosslinked GelMA networks can be controlled by adjusting the light intensity and exposure time where LAP is abundant in the photophysical reaction.

The photo-crosslinking reactions should occur in an area of light exposure to ensure that the materials get crosslinked immediately and reach a density to maintain the shape. As shown in the flowchart in Fig. 4, the printing resolution depends on the photo-crosslinking rate and density, which are controlled by the production rate and the number of free radicals. Thus, adjusting the light intensity and exposure time directly control the crosslinking region. A light absorber is incorporated to change light intensity distribution to adjust the curing depth. In addition to parameter adjustments, the crosslinking density also depends on the GelMA concentration and the substitution of GelMA, which is determined by the number of C=C double bonds. Here, the influence

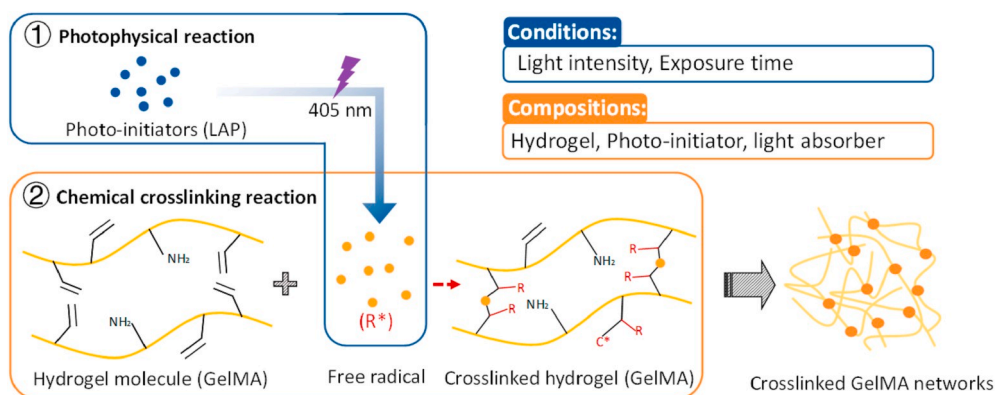


Fig. 3. Schematic diagram of the photo-crosslinking reactions. Photophysical reaction (1) and chemical crosslinking reaction (2) occurring in the photo-crosslinking process.

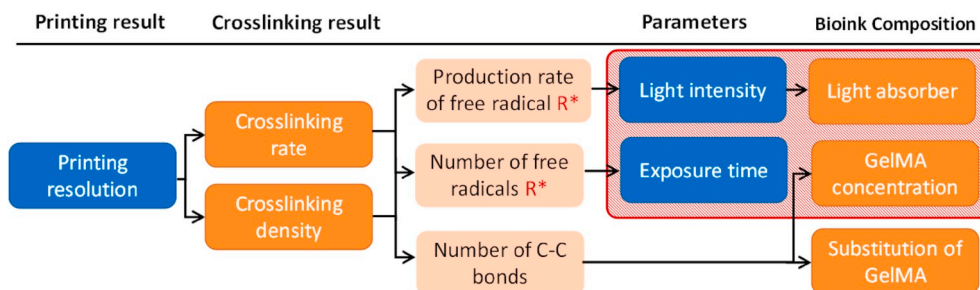


Fig. 4. Flowchart of the PBP control. The printing parameters and the bioink composition (in the red frame) influence the printing results.

of the printing parameters (light intensity, exposure time) and bioink composition (GelMA concentration, light absorber concentration) are investigated to determine printability during PBP. Their influences are listed in Table S1.

3.4. Relationships between rheological behavior and printability

It is costly and time-consuming to optimize the parameters using only printing experiments. Thus, it is crucial to characterize printability before printing. A photorheological test was used to characterize the photo-crosslinking properties of the bioink; the results are shown in Fig. 5A. The storage modulus G' and loss modulus G'' are recorded as the bioink is crosslinked under light exposure. The storage modulus G' expresses the capability to store elastic deformation energy of viscoelastic materials, reflecting the stiffness of the material. The loss modulus G'' describes the loss of energy during viscous deformation, reflecting the material's viscosity [39–41]. The intersection of the G' and G'' curves is generally considered the gel point of the material. The time from the beginning of the exposure to the gel point is referred to as the gel time (GT).

It is crucial during PBP to separate the printed structure from the uncured bioink to achieve high printing resolution. A high stiffness of the printed structure and low viscosity of the uncured bioink are desirable for high-precision printing. We define " $\Delta G'$ ", as shown in Fig. 5A, as the difference in the G' value of the crosslinked and uncrosslinked states on the log scale to express the rheological differences between the printed structure and the uncured hydrogel. As the exposure time increases, the degree of crosslinking of the bioink increases until crosslinking is complete; thus, the value of $\Delta G'$ increases and eventually stabilizes. Since $\Delta G'$ reflects the crosslinking density of the material, the time to reach this point is the crosslink time. Getting completely crosslinked is time-wasting, after conducting numerous PBP tests with the GelMA, we believe that 75%–80% of the $\Delta G'$ log value in the diagram is a suitable range to obtain the optimum crosslinking density during PBP. The corresponding exposure time range is referred to as the printable window, as shown in Fig. 5A.

On the other hand, maintaining the printed shape requires higher elasticity than viscosity. The bigger the difference between G' and G'' , the better the shape retention is. The index " ΔM " is defined as the difference between the G' value and G'' value on the log scale after full exposure during PBP. The value of ΔM gradually increases from the gel point, indicating that the GelMA molecules have crosslinked, and the degree of crosslinking is increasing under light exposure. A large value of ΔM means that the printed structure behaves more like an elastomer than a viscous one. $\Delta G'$ and ΔM are rheological parameters that depend on the bioink.

The results of the rheological test are shown in Fig. 5B–D. In Fig. 5B, the viscosity of different GelMA concentrations was tested. At concentrations below 10% w/v, the viscosity of GelMA was as low as that of commercial resin, and it had good fluidity. Reducing the viscosity of bioink is beneficial for improving the printing efficiency and increasing the deformation of the printed structures immersed into the bioinks.

As the GelMA concentration increased from 5% to 10%–20%, the value of G' increased, and the GT decreased from 80.1 s to 17.1 s (Fig. 5C). The crosslinking probability of the C=C double bonds of the GelMA molecules substantially increased, and the crosslinking density and efficiency increased. A high concentration of the GelMA bioink resulted in a high crosslinking density and high crosslinking rate, improving the PBP performance. In contrast, poly (ethylene glycol) diacrylate (PEGDA) was tested under the same condition. The G' value of PEGDA was similar to GelMA, but the GT was much faster. Moreover, the G' value of PEGDA increased rapidly, reaching the maximum at 40 s of exposure and remaining at that value, whereas the G' value of the GelMA increased more slowly, requiring 180 s to reach the peak value. The crosslinking efficiency of PEGDA was much higher than that of the GelMA; thus, the PEGDA had better printability than the pure GelMA.

The light absorber tartrazine was added to control the light intensity in the GelMA system to improve printability. The rheological properties of the GelMA-based bioink with concentrations of 0%, 0.5%, and 1.0% w/v tartrazine were measured to evaluate the influence of the absorber, as shown in Fig. 5D. As the tartrazine concentration increased, the GT was prolonged, and the value of G' decreased, indicating that the light absorber contributed to decreasing the crosslinking rate and crosslinking density, adversely affecting the shape retention of the printed products. These results were consistent with the analysis of the photo-crosslinking mechanism.

The larger the $\Delta G'$ value, the higher the printing precision is due to the higher crosslinking density of the hydrogel. A higher $\Delta G'$ allows for better separation of the cured parts from the uncured bioink and easier removal of the residual bioinks from the printed product. It is necessary to obtain a balance between viscosity and elasticity for ΔM . Increasing the GelMA concentration increases the crosslinking density and the elasticity of the material, whereas the viscosity increases much faster. Fig. 5Dii shows that the viscosity decreased, and the elasticity remained nearly unchanged as the light absorber concentration increased. However, if the light absorber concentration is too high, the crosslinking density decreases rapidly, leading to a decrease in ΔM . Numerous printing trials have shown that the value of ΔM should be in the range of 1.5–2.0. Beyond this range, the elasticity is low, and the viscosity is high (making it difficult to separate the cured structure from the bioink). Below this range, the elasticity is low, and the velocity is much lower (difficulty in crosslinking). Thus, the crosslinking properties of GelMA can be determined from the rheological curves of G' and G'' rather than using printing trials to determine the printing ability.

Therefore, the photorheological evaluation of the prepared GelMA bioink can be conducted before PBP to obtain the diagram of the G' and G'' curves. The higher the value of $\Delta G'$, the higher the printing resolution is. The parameter values can be approximated using the printable window in the graph, and the stiffness can be estimated from the value of ΔM . The viscosity of the bioink significantly affects the printing efficiency. Low viscosity results in high fluidity, enabling the bioink to fill the gaps rapidly and avoid structural deformation.

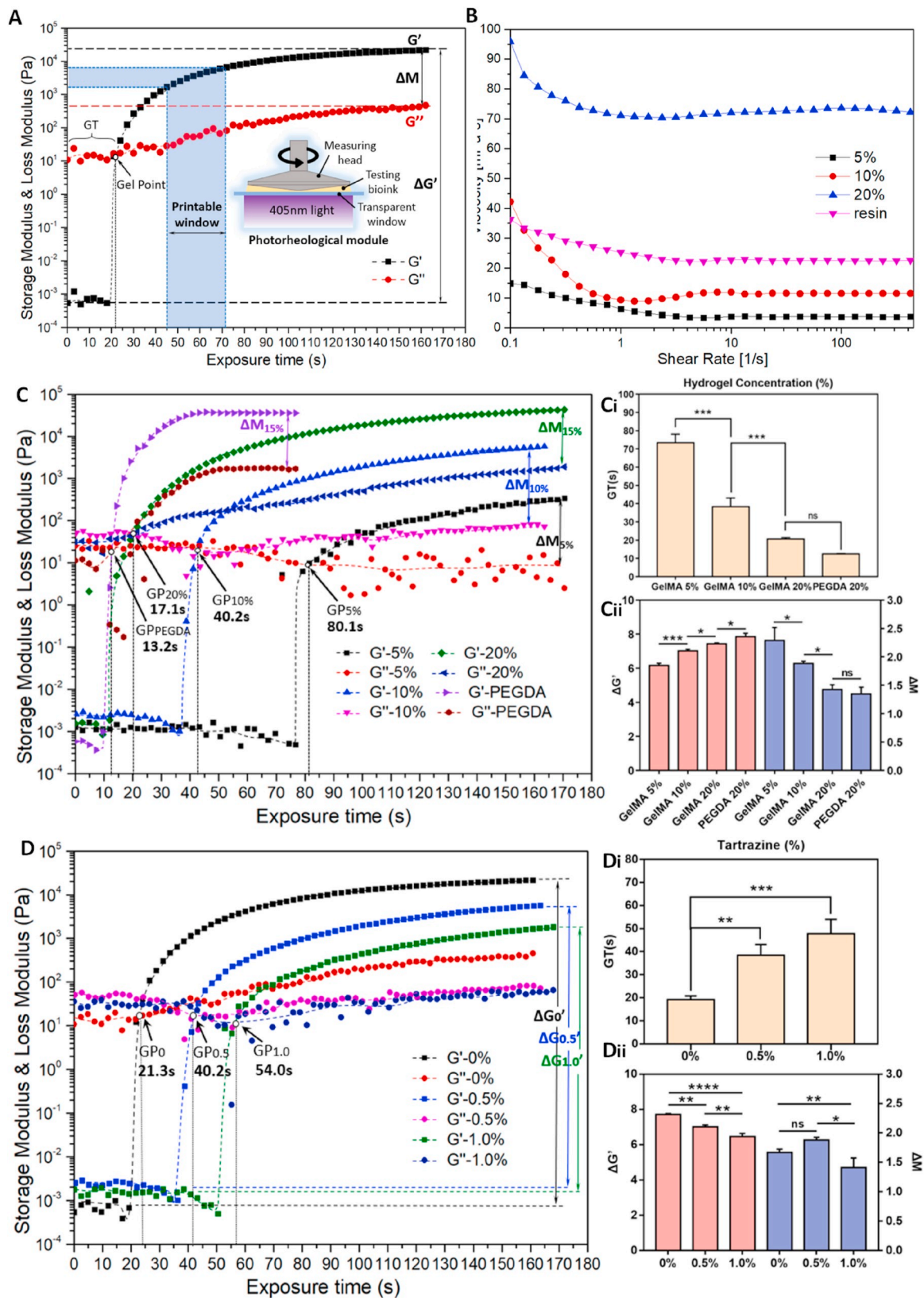


Fig. 5. The requirements of bioinks determined by photoreheological characterization. A) Schematic diagram of the analysis of the storage modulus (G') and loss modulus (G'') in the photoreheological module, “ $\Delta G'$ ” is the difference in the G' value of the crosslinked and uncrosslinked states on the log scale, “ ΔM ” is the difference between the G' value and G'' value on the log scale after full exposure; B) viscosity comparison of different concentrations of GelMA and commercial resin; C) storage modulus and loss modulus of gelatin methacryloyl (GelMA) and poly (ethylene glycol) diacrylate (PEGDA); gel time (Ci), ΔM , and $\Delta G'$ of the materials (Cii); D) storage modulus and loss modulus of GelMA with different tartrazine concentrations, gel time (Di), ΔM , and $\Delta G'$ of tartrazine (Dii).

4. Printing analysis

The essence of 3D bioprinting is to modulate the photo-crosslinking reactions with engineering methods. The reaction conditions are controlled by digital techniques. In this process, the relationship between the reaction conditions and the printing process should be analyzed to control the printing conditions and products. It is vital to analyze the photo-crosslinking process and the manufacturing errors during PBP.

4.1. Photo-crosslinking control under patterned light

During PBP, when the light is incident on the material, the crosslinking reactions occur in areas exposed to the light, as shown in Fig. 6A. The patterned light projected in PBP is composed of millions of pixelated lights, which can be regarded as points of light. The photo-crosslinking control of patterned light is based on the photo-crosslinking control of the point lights.

4.1.1. Photo-crosslinking control of a point of light

The schematic in Fig. 6Ai–Aiii shows the light intensity in a material system under a point of light. The light intensity is expressed with different colors; red indicates high intensity, orange indicates medium intensity, and yellow means low intensity. As a point of light penetrates the bioink, the light intensity in Fig. 6Aii has a Gaussian distribution. The light intensity diminishes along the periphery from red to yellow. The crosslinking density decreases from the red region to the yellow region; the bioink in the red region has been crosslinked, whereas that in the yellow region has been crosslinking, but the density is too low to support the structure. As the exposure time increases, the curing region expands in the depth and width directions.

The curing depth should be slightly larger than the layer thickness to ensure good bonding between printed layers. The crosslinking density of the interface between the printed layers needs to be in the red region to ensure reliable bonding. The curing depth can be adjusted precisely using the light attenuation theory in a colored material system [42–44].

4.1.2. Photo-crosslinking regulation under several points of light

If all light points have the same intensity, the curing region is the

same. When the bioink is exposed to a point of light, there is only one curing region, as shown in Fig. 6Bi. Exposing discrete points of light will lead to three identical curing regions (Fig. 6Bii), when these three points of light are far enough apart not to affect each other. However, when the points of light are in close proximity, the curing regions connect, expanding the curing depth (blue shaded area) rather than having discrete curing regions (red area), as shown in Fig. 6Biii [45,46]. We assume that the illumination of the light point is affected by others when the light points are close, leading to an increase in the curing depth. The degree of increase is directly related to the number of light points. We believe that this phenomenon substantially affects the printing results. During one-layer PBP, the bioink is exposed to a patterned light, and the curing depth depends on the shape of the light pattern. A non-uniform projected light pattern results in a non-uniform curing depth and broken structures (parts are over-cured while other parts are under-cured).

The amplification mechanism is unclear, but it significantly affects the printing resolution. It is nearly impossible to print a granule with a point of light under limited optical resolution because the light energy of the light point is too low to cure the bioink. A single line consisting of several light points is also difficult to fabricate for the same reason. Although expanding the line width or increasing the light intensity will improve the results, the printing resolution is limited.

4.2. Analysis of printing errors

Printing errors refer to differences between the printed result and the design model and are inevitable during printing. Light scattering and over-curing in the depth direction are two main reasons for printing errors. It is vital to understand the reason for the printing errors to eliminate them and improve the printing precision. Since PBP is a layer-forming process, printing errors primarily occur in one layer, and the interface between the layers and are referred to as 2D and 3D printing errors, respectively. As mentioned above, the printing resolution can be controlled by the GelMA concentration, light absorber, and printing parameters (i.e., light intensity and exposure time). The same goes for the printing errors. Two standard models are designed to obtain quantitative measurements, and the influences of these factors are investigated.

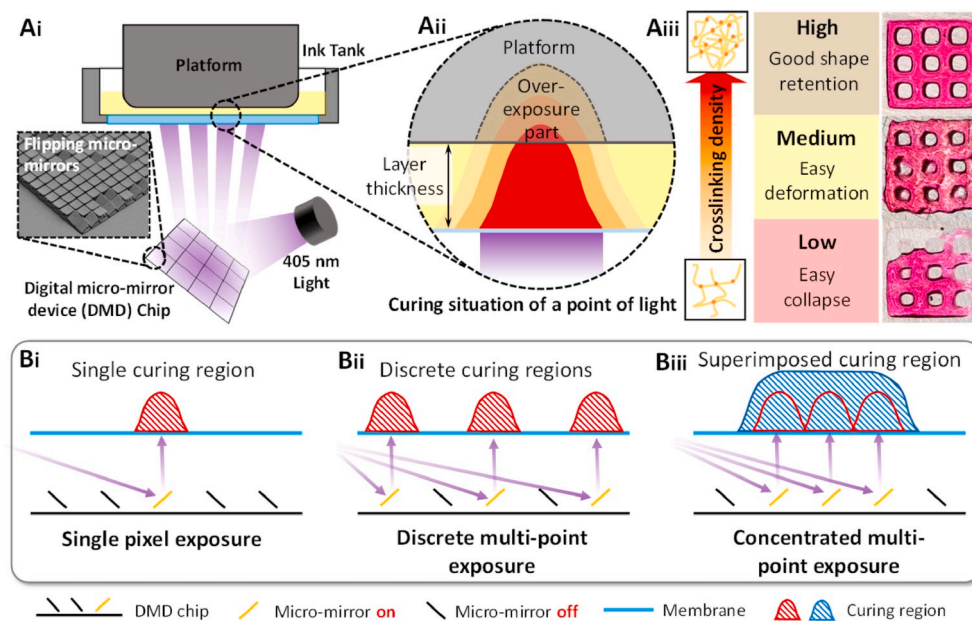


Fig. 6. Schematic diagram of the crosslinking processes under patterned light. Ai) & Aii) Photo-crosslinking regulation under a point of light; Aiii) Cured GelMA with different crosslinking densities; Bi) Schematic diagram of crosslinking under a single-point light; Bii) Schematic diagram of crosslinking under discrete multi-point lights; Biii) Schematic diagram of superimposed crosslinking under concentrated multi-point lights.

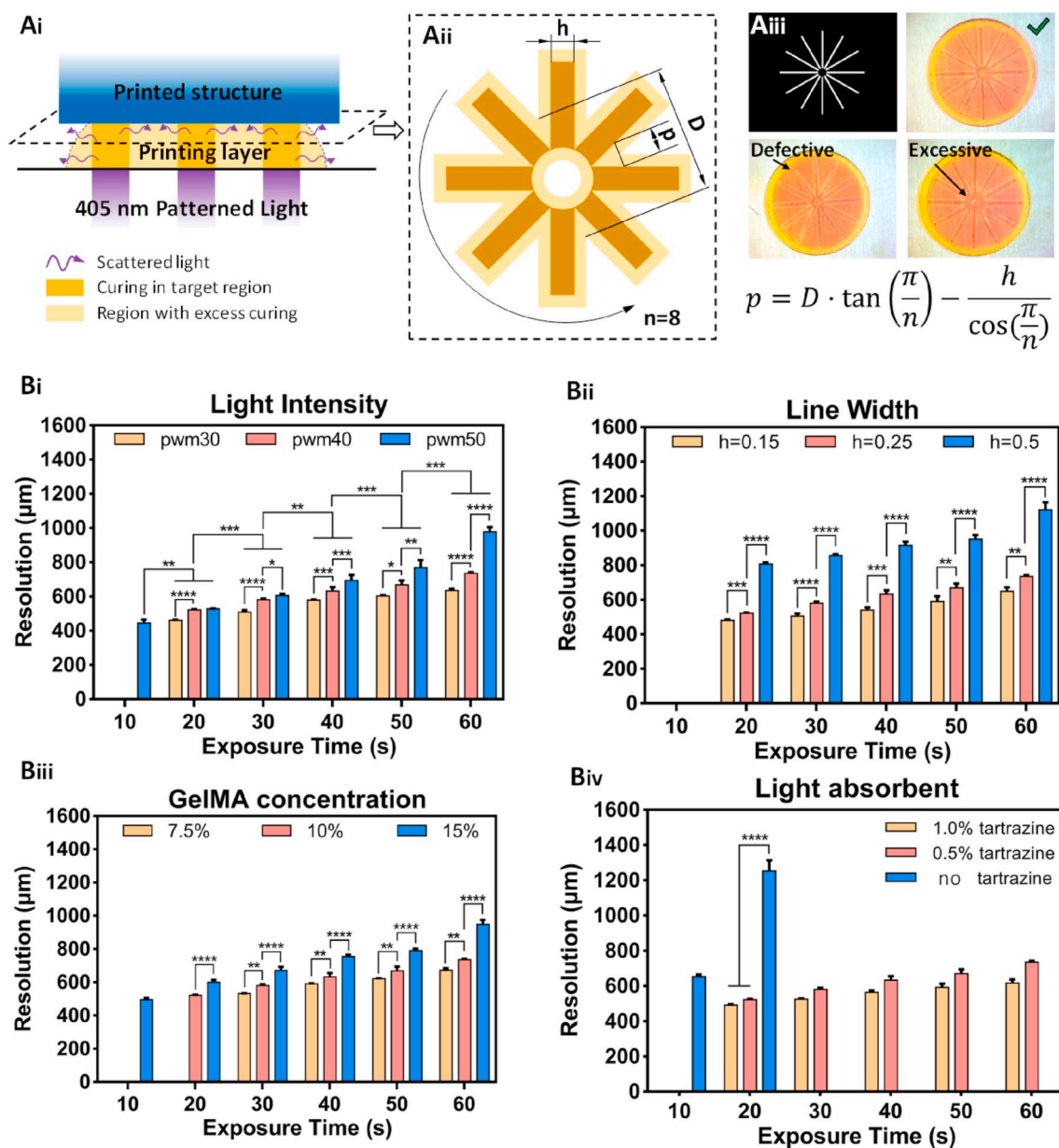


Fig. 7. Schematic diagram of the 2D printing analysis. Ai) schematic diagram of the 2D printing error caused by light scattering; Aii) the “spokes” model for measuring the 2D printing error (“p” is calculated by measuring “D”, which is the diameter of the circle of the cross points; “n” is the number of lines, and “h” is the line width.); Aiii) images of the printed spokes and the equation; Bi) the printing resolution of 10% GelMA and 0.5% tartrazine at different light intensities controlled by PWM (30, 40, and 50) for increasing the exposure time; Bii) the printing resolution of 10% GelMA and 0.5% tartrazine at different line widths (0.15, 0.25, and 0.50 mm) for increasing the exposure time; Biii) the printing resolution of different GelMA concentrations (7.5%, 10%, and 15%) and 0.5% tartrazine for increasing the exposure time; Biv) the printing resolution of 10% GelMA for different tartrazine concentrations (0, 0.5%, and 1.0%) for increasing the exposure time.

4.2.1. Analysis of 2D printing errors

2D printing errors refer to excessive curing beyond the exposed areas, leading to poor printing resolution in each layer. These errors occur within one layer and are caused by light scattering. The schematic diagram of a 2D printing error is shown in Fig. 7Ai. The patterned light is projected on the bottom of the ink tank and is scattered in the plane direction due to the inhomogeneity of the cured GelMA. After being exposed to scattered light, the GelMA beyond the exposed areas is crosslinked, resulting in 2D printing errors.

The degree of light scattering is affected by the hydrogel molecule size, the degree of crystallinity, and the phase separation [47–49]. Light scattering is inevitable and cannot be avoided, but we can decrease the influence by adding a light absorber to the bioink. The intensity of scattered light depends on the intensity of incident light but is much

lower. Photopolymerization occurs only when the light energy reaches a threshold value. Thus, it is efficient to improve the printing resolution by reducing the intensity of scattered light below the threshold value with a light absorber. It is worth mentioning is that the addition of a light absorber reduces the intensity of the scattered light as well as the intensity of incident light, leading to the decrease in the crosslinking rate and density. Besides, different GelMA concentrations produce different curing results according to the analysis of the photo-crosslinking mechanism. A high concentration of GelMA improves the mechanical strength of the printed structure but also increases the degree of excessive curing.

An in-plane model with a “spoke structure” was proposed to evaluate the printing results quantitatively and optimize the printing parameters (Fig. 7Aii). Since hydrogel structures are weak and soft and can be

deformed by contact, the printed patterns are observed and recorded with a microscope. Due to the influence of light and shadow under a microscope, the widths of the lines are difficult to measure. However, in the spoke structure, the lines touch each other at one end and radiate outward at the other end, and the widths expand after exposure printing, increasing the diameter of the circle at the intersection of the lines. To normalize the printing results, the parameter “p” is defined as the printing resolution in the X–Y plane, i.e., the distance between the printed lines and the designed lines, as shown in Fig. 7Aii. Thus, the resolution “p” can be calculated as follows: $D \cdot \tan\left(\frac{\alpha}{n}\right) - \frac{h}{\cos\left(\frac{\alpha}{n}\right)}$. The

printing results are displayed in Fig. 7Aiii.

The influences of the light intensity, GelMA concentration, and light absorber concentration are investigated systematically; the results are shown in Fig. 7Bi–Biv. The exposure time is the most commonly used parameter to adjust the printing results and is used to fine-tune the printing precision. The light intensity is controlled by pulse-width modulation (PWM) in this research, and the values of PWM 30, 40, 50 correspond to the intensities of 3, 4, and 5 mW cm⁻², respectively. The effect of the light intensity of the printing results are shown in Fig. 7Bi. Increasing the light intensity enhances the resolution “p” and decreases the printing precision. The effects of the light intensity are more pronounced during long exposures (60 s) than short exposures (20 s). This result shows that GelMA was not completely crosslinked during the short exposure time, regardless of the strong light intensity. Thus, we can obtain high printing resolution with strong light intensity and a short exposure time. Moreover, a very low concentration of GelMA causes crosslinking failure, whereas a high concentration results in printing errors, as shown in Fig. 7Biii. A high concentration of GelMA results in a precise structure due to the tightly crosslinked network. Generally, the concentration of GelMA depends on the biological or mechanical requirements of specific applications. As shown in Fig. 7Biv, the effects of the tartrazine are significant. We did not obtain the results of the printed samples with no tartrazine, but the printing resolution was effectively controlled by adding 0.5% and 1.0% of the light absorber. There is no significant difference between a tartrazine concentration of 0.5% and 1.0%; the likely reason is that a 10% GelMA concentration provides sufficient crosslinking density. Adding a light absorber is not suggested for bioinks with a GelMA concentration below 7.5% w/v.

Besides, as mentioned above, the degree of light scattering is affected by the line width. Spoke structures with line widths of 0.15 mm, 0.25 mm, and 0.5 mm were printed under the same conditions with the same bioink. As depicted in Fig. 7Bii, the printing resolution is significantly higher at 0.5 mm than at 0.15 mm and 0.25 mm, and the spoke structures cannot be printed at 10 s exposure due to insufficient curing. The results show that a large printing area requires a low crosslinking degree with low light intensity or a short exposure time, whereas an ultrafine

pattern (a filament or tiny point) requires a high light intensity with a short exposure time to ensure sufficient printing resolution. A summary of the influences of these parameters and the reasons are listed in Table 1. Table S2 shows examples of printed surgical dressing and a face mask using the described print parameters.

4.2.2. Analysis of 3D printing errors

3D printing errors refer to errors or inaccuracies in the vertical direction. These are caused by overcuring of the bioink in the depth direction. It is necessary to adjust the curing depth slightly higher than the layer thickness to ensure good bonding between the layers in PBP, but too much over-curing leads to 3D printing errors, decreasing the surface quality.

The control of the curing depth of each layer is crucial to prevent 3D printing errors. As shown in Fig. 8Ai, the light pattern is projected on the bottom of the tank, and the intensity of light decreases with the depth. The bioink is crosslinked in areas exposed to the light, and the crosslinking density of GelMA decreases as the light intensity decreases. A high crosslinking density is required at the interface of the printed structure and the printing layer to ensure bonding between layers. Due to the low solid content of the bioink, the crosslinking density is typically not sufficient, resulting in the collapse and deformation of the printed structure. Thus, we have to increase the concentration of the bioink or enhance the exposure conditions (light intensity and exposure time) to increase the crosslinking density, which inevitably increases the curing depth. The printing parameters (light intensity and exposure time) and the concentration of GelMA and tartrazine are investigated systematically in this research to improve the printing performance and reduce curing errors. It has been shown that adding a light absorber such as tartrazine is effective in ensuring an accurate curing depth [44].

Beams or lateral structures have been proposed to investigate the effects of different parameters on the curing depth [43]. Since hydrogel bioinks are soft and deformable, significant errors may occur during measurements due to contact, water loss, or air exposure. Here, we proposed a “winding stair” structure as a standard model to measure the curing depth quantitatively, as shown in Fig. 8Aii. In the “winding stair” structure, a rotating slope was designed to form the over-curing region; the printed thickness of the winding stair structure was larger than the designed thickness. A schematic diagram of the side view of the winding stair is depicted in Fig. 8Aiii. The structure was sliced into layers, and “Dc” is the curing depth. The dashed line denotes the outline of the printed winding stair. The intersection plane of the printed slope and the surface is a fan-shaped pattern with the angle “α”, as shown in the section view P–P of Fig. 8Aiii. Thus, the measurement error is reduced significantly by transforming the depth into the angle “α”. The curing depth “Dc” is calculated as $Dc = L \cdot \frac{\alpha}{2\pi} - t$, where “L” is the rise of the winding stair (see Fig 8Aiii).

The influence of the printing parameters and concentrations on the

Table 1
The influence factors of 2D printing errors.

| Influence factors | Exposure time | Light intensity | Tartrazine concentration | GelMA concentration | Line widths h | Number of spokes n |
|-------------------|--|--|---|---|--|---|
| Degree | *** | ** | **** | *** | *** | ns |
| Influence reasons | Long exposure time increases the light energy and expands the curing region. | The light intensity affects the crosslinking rate. | The light absorber consumes the energy of the incident light, preventing over-curing due to light scattering. | A high concentration provides more crosslinking sites, increasing the crosslinking density. | A wider line increases the exposure area and light scattering. | More spokes result in a larger diameter but do not influence the printing resolution. |

curing depth for different exposure times are shown in Fig. 8Bi–Biv. The exposure time is regarded as an adjustable parameter to control the printing results. As shown in Fig. 8Bi, the effect of the light intensity on the curing depth is greater than that of the 2D resolution, and changing the light intensity and exposure time have a large effect on the curing depth. The GelMA concentration significantly affects the 3D structure. A low concentration provides fewer GelMA monomers, resulting in a weak crosslinking network. The results in Fig. 8Biii show that a 7.5% concentration of GelMA is not suitable for 3D structures. There are significant differences in the curing depth for different GelMA concentrations. The tartrazine concentration has a strong effect on the curing depth. As shown in Fig. 8Biv, the curing depth is extremely large when no tartrazine is added, even for a short exposure. On the other hand, when 1.0% w/v of the light absorber is added, the curing depth stabilizes near 250 μm , regardless of the exposure time. The thickness is a crucial parameter for printing 3D structures and has to match the curing depth. For instance, a curing depth of 200 μm results in high printing quality for a thickness of 100 μm but significant printing errors for 50 μm thickness. The curing depth accumulates larger when printing occurs layer by layer, significantly increasing the 3D printing error, as depicted in Fig. 8Bii. A summary of the influences of these parameters and the reasons are listed in Table 2. Table S3 shows two examples of microneedles and a nerve conduit printed using the described parameter configuration.

For further improvements in the printing accuracy, we have to increase our understanding of points of light and improve the hydrogel properties to achieve a high crosslinking density, a high crosslinking rate, and excellent bio-performance.

4.3. The printing strategies of PBP

High-quality conventional structures, such as cylinders, cubes, and other geometrical structures can be easily printed. However, most bio-printed 3D structures have a complex curved surface (e.g., ear, nose, and heart) or specific features (e.g., microchannels) required for biomedical applications. Some require a custom design. The manufacturing of these structures remains a significant challenge. PBP is a potential technique to print these structures, but a standardized printing protocol is lacking. We focus on structures commonly used in biomedical applications and divide them into five basic types based on the slice shape used in PBP. Five printing strategies are proposed for the five structures, as shown in Table 3. The features and applications of these structures are analyzed to determine the bioink composition, and the printing difficulties are pointed to select the appropriate printing parameters. An approximate range of the printing parameter values is suggested for printing trials. We hope that these printing strategies will help to promote the use of PBP technology.

4.3.1. Printing strategies for solid structures

Solid structures have no internal cavities and are the easiest structures to fabricate using PBP. The slice shapes are relatively uniform. The

most common printing error is related to the internal shrinkage of the cured bioink. Therefore, a strategy to reduce internal shrinkage is to ensure low photo-crosslinking density to maintain the shape of the produce. Low light intensity or short exposure time and a low monomer concentration are suitable for printing solid structures, such as cell-laden printing.

4.3.2. Printing strategies for vascular structures

Vascular structures have complex internal channels. The slices of vascular structures commonly have holes or microchannels, and the non-exposure area is smaller than the exposure area. When printing vascular structures, it is desirable to achieve a balance between maintaining the patency of channels and the integrity of the final product. Due to the combined effects of light intensity and light scattering, vascular structures are easily blocked and challenging to print. Therefore, the printing strategies must be adapted to the structural features of the channels. A high light absorber concentration is required to prevent over-curing due to light scattering and maintain the patency of channels. Besides, high light intensity and a short exposure time are adopted to ensure crosslinking of the GelMA hydrogel. This strategy results in a small curing depth; thus, thin layers are required.

4.3.3. Printing strategies for conduit structures

The conduit structures are tubular with perforated holes, and the height is typically larger than the cross-section. The slices are uniform, with no lateral features. The most common difficulty of printing conduit structures successfully is that the perforated holes are filled easily by the material. The GelMA hydrogel is trapped in the perforated holes due to the capillary action in the consecutive printing of the layers. Without the circulation of the GelMA bioink, the molecular weight of the GelMA hydrogel will increase over time. The best strategy to prevent this problem is to decrease the light intensity and the exposure time; thus, low light intensity and large layer thickness are required. A high GelMA concentration is used to ensure a high crosslinking rate, and a low concentration of the light absorber tartrazine is used to improve the curing depth and match the layer thickness.

In addition, the slice shape also affects the printing results. Due to the superimposed pixel lights, the light intensity is non-uniform in different slice areas, resulting in a non-uniform curing depth in the layer, with overexposure in some areas and underexposure in others. As a result, a low light intensity may lead to defects in the printed structure, as shown in Fig. S1. Thus, the cross-sectional shape of the conduit structure has to be designed carefully. The exposed areas and the holes should be uniformly distributed.


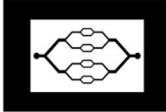



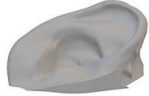
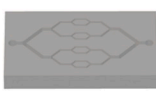

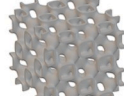
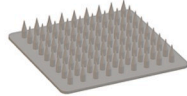
4.3.4. Printing strategies for thin-walled structures

Thin-walled structures, such as porous scaffolds, are relatively delicate. The exposed area is much smaller than the non-exposed areas are in the slice, leading to an insufficient exposure dose, which is the main reason for the printing failure of this type of structure. Thus, the best

Table 2
The influence factors of 3D printing errors.

| Influence factors | Exposure time | Light intensity | Tartrazine concentration | GelMA concentration | Thickness h |
|-------------------|---|---|---|---|---|
| Degree | *** | ** | **** | *** | *** |
| Influence reasons | A long exposure time increases the light energy and expands the curing depth. | The light intensity affects the curing depth. | The light absorber consumes the energy of the incident light to prevent over-curing in depth. | A high concentration provides more crosslinking to increase the crosslinking density. | A small thickness results in more printing layers and a greater curing depth. |

Table 3
Suggested printing strategies for five types of structures used for specific applications.

| Structure types | | | | |
|---|--|--|---|---|
| Solid structures | Vascular structures | Conduit structures | Thin-walled structures | Microcolumn structures |
|  |  |  |  |  |
| Applications | | | | |
|  |  |  |  |  |
| Implants: ear | Large-scale organoids with internal channels | Neural scaffolds | Bionic scaffolds | Surface microstructures |
| Structure features | | | | |
| Complex surface No inner features Large volume | Complex channels within structure | Height is large with perforated holes Same cross sections | Large height Thin and uniform exposure area | Flat structure Tiny and array point High mechanical property is required |
| Difficulties | | | | |
| Deformation caused by internal shrinkage | Forming with unblocked channels | Forming with unblocked holes | Defects/deformation caused by incomplete crosslinking | Array defects caused by lack of curing/over-curing between columns |
| Printing analysis | | | | |
| Exposed area is large; Low crosslinking density is required. | Exposed area is much larger than uncured area. Less thickness is required. | Uncured hydrogel tends to stay in the holes blocking the holes. | High exposure is required for sufficient curing. | Large curing depth, low light scattering, and high crosslinking density are required to achieve good mechanical properties |
| Parameter selection | | | | |
| <ol style="list-style-type: none"> 1. Low GelMA concentration (5%-10%); 2. High light absorber concentration; 3. Low exposure (low light intensity/short exposure time); | <ol style="list-style-type: none"> 1. Medium GelMA concentration (10%-15%); 2. Appropriate light absorber concentration to achieve small curing depth; 3. High light intensity and short exposure time; | <ol style="list-style-type: none"> 1. Medium GelMA concentration (10%-15%); 2. Low light absorber concentration to achieve large curing depth; 3. High light intensity and short exposure time to achieve low light scattering; | <ol style="list-style-type: none"> 1. High GelMA concentration (12%-18%); 2. Appropriate light absorber concentration to achieve a smooth surface; 3. High exposure (high light intensity/long exposure time); | <ol style="list-style-type: none"> 1. High GelMA concentration (12%-18%); 2. Low light absorber concentration to achieve a large curing depth; 3. High exposure (high light intensity/long exposing time); |

strategy is the overexposure of each layer to ensure shape retention by increasing the crosslinking density. High exposure doses are applied when printing thin-walled structures to achieve an appropriate crosslinking rate because structural damage may be caused by underexposure.

Another problem is the printing resolution of thin-walled structures, including the printing resolution of the structure and the resolution of the internal pores, i.e., the minimum size of the thin walls and internal pores is critical. The printing resolution is closely related to the photocuring characteristics of the material. The ideal photocuring material can perfectly reproduce the size and resolution of the designed model. However, due to the low photocuring rate and low optical crosslinking density of current hydrogel materials, such as GelMA, thin-walled structures must be fabricated by minimizing over-curing, which inevitably reduces the printing resolution. The pores of thin-walled structures are typically interconnected, which is conducive to the circulation of bio-ink, minimizing blockages.

4.3.5. Printing strategies for microcolumn structures

Microcolumn structures and thin-walled structures have similar characteristics. The exposure areas are small and discrete, the arrays and columns may be in close proximity, and the microcolumns generally have low height. The printing strategies of microcolumn structures are different from those of thin-walled structures because over-exposure occurs at high exposure doses, leading to excess curing between the columns. A large curing depth is required to prevent printing defects due to light scattering; thus, a low light absorber concentration (high light intensity or a long exposure time) is necessary. A high GelMA concentration is needed for fabricating microneedles due to the required high crosslinking density. Microcolumn structures are typically microarrays used to analyze cell behavior and microneedles for drug delivery and signal detection.

The printing parameters and GelMA hydrogel concentrations suitable for the five types of structures are listed in [Table S4](#).

Porous structures that mimic the shape of scaffold models were designed to verify the applicability of the proposed printing strategies. The slices of these structures included a grid pattern (conduit structure)

and small square arrays (microcolumn structure). The following printing strategies were used: 15% GelMA concentration, 0.5% tartrazine concentration, a light intensity of 5 mW cm^{-2} (PWM 50), with 30 s for the conduit structure and 50 s for the microcolumn structure. The printed results are displayed in Fig. 9. The structures exhibit no defects and have fine perforated pores.

5. Characterizations of printed hydrogel scaffolds

Human Umbilical Vein Endothelial Cells labeled with a Green Fluorescent Protein (GFP-HUVECs), purchased from Suzhou Intelligent Manufacturing Research Institute (Suzhou, China), were seeded on the porous GelMA scaffolds to verify the biocompatibility of the printed structures. As shown in Fig. 10A, after 1, 4, 7, and 10 days of cultivation, the cells adhered to the scaffolds and spread on the surface of the porous

scaffolds over time. After 10 d, the entire scaffold was covered by the HUVECs. Furthermore, we seeded the HUVECs on scaffolds with and without fine pores. The optical density (OD) value obtained from the CCK-8 kit is shown in Fig. 10B, indicating that the porous structure accelerated the proliferation rate of HUVECs. Our results demonstrate that the printed porous GelMA hydrogel scaffolds have excellent biocompatibility for culturing cells in-vitro. We observed in Fig. 10Cii that the growth of the HUVECs occurs in a specific direction, which can be attributed to the small grooves on the surface of the printed structures. The excellent bio-performance of these complex scaffolds with fine pores indicates a significant potential of the method for stem cell proliferation.

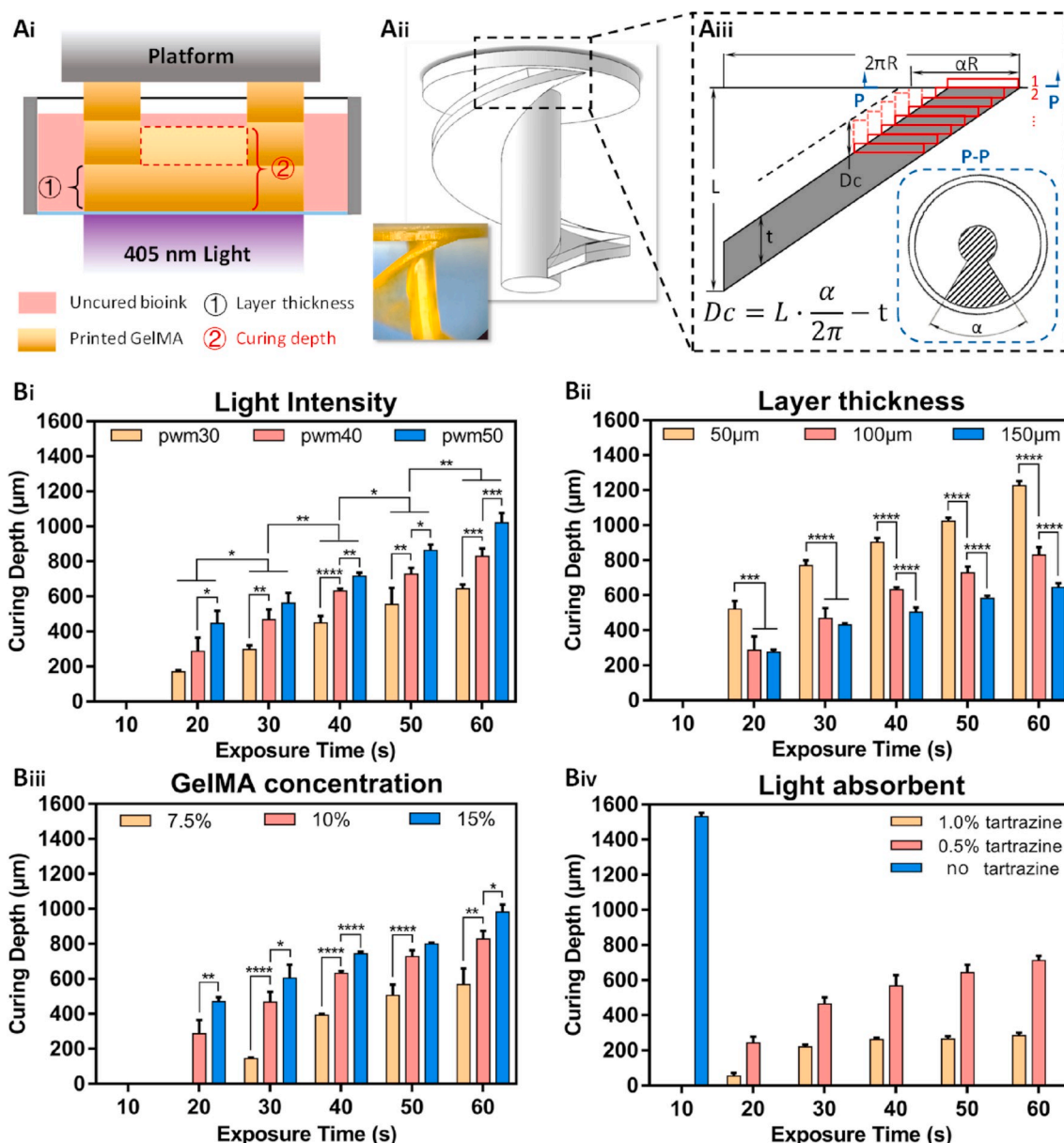


Fig. 8. Schematic diagram of the 3D printing analysis Ai) schematic diagram of the printing error caused by light penetration; Aii) the axonometric diagram of the “winding stairs” model to measure the 3D printing error; Aiii) the schematic diagram of the unfolded winding stairs for the analysis; Bi) the printing resolution at different light intensities for PWM 30, 40, and 50 (corresponding to 3, 4, and 5 mW cm^{-2}) for increasing exposure times; Bii) the printing resolution at different line widths (50, 100, and $150 \mu\text{m}$) for increasing exposure times; Biii) the printing resolution of different GelMA concentrations (7.5%, 10%, and 15% wt) for increasing exposure times; Biv) the printing resolution of 10% GelMA hydrogel for different tartrazine concentrations (0, 0.5%, and 1.0% wt).

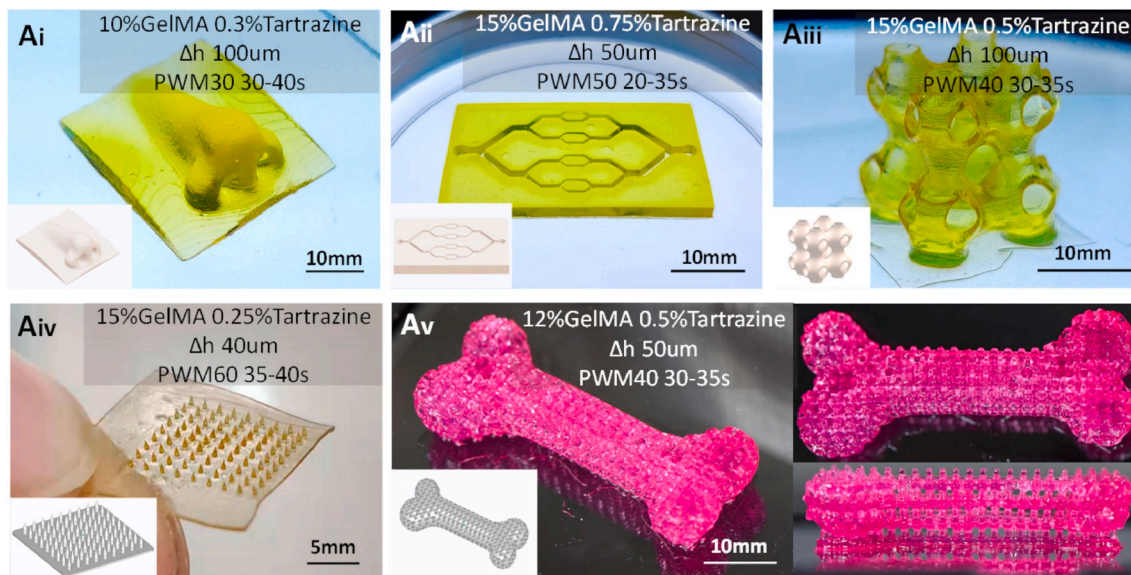


Fig. 9. The printed GelMA structures fabricated with the proposed printing strategies. Ai) printed solid structure (nose); Aii) printed vascular structure (angiogenesis model); Aiii) printed thin-walled structure (porous lattice scaffold); Aiv) printed microcolumn structure (microneedle); Av) printed composite structure (porous bone) fabricated by combining the printing strategies of the conduit structure and the microcolumn structure.

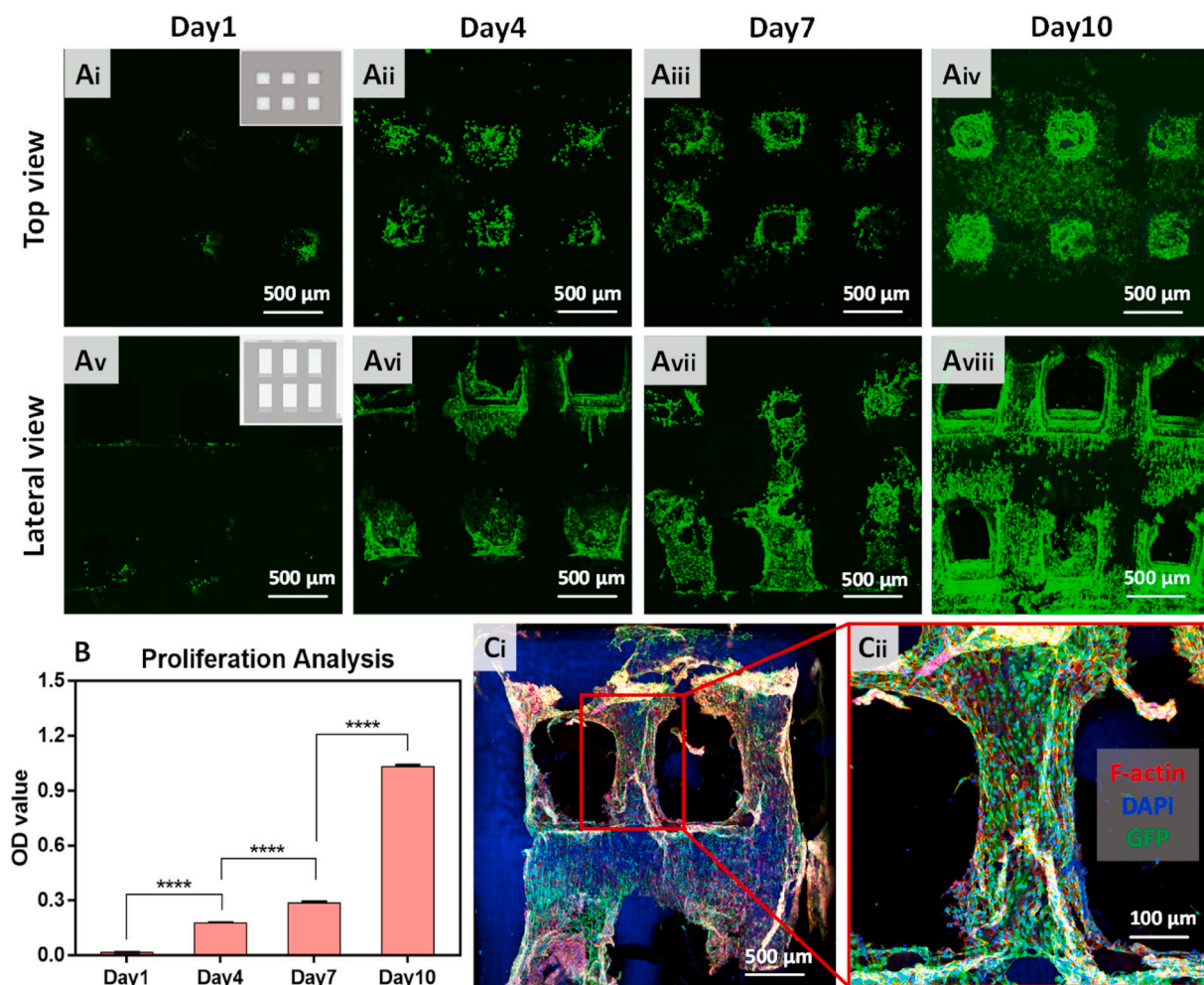


Fig. 10. Biocompatibility of the printed porous scaffolds. (A) Top view of cell growth on scaffolds on (i) day 1, (ii) day 4, (iii) day 7, and (iv) day 10. Side view of cell growth on scaffolds on (v) day 1, (vi) day 4, (vii) day 7 and (viii) day 10. (B) Cell proliferation rate on days 1, 4, 7, 10 displayed with the optical density (OD) value. (C) Confocal image of HUVECs on the porous scaffolds (the image on the right shows a magnification of the selected area).

6. Discussion

Printability of bioinks is an abstract concept in 3D printing that describes the precision level of the manufacturing process. A clear standard for printability is currently lacking. This research analyzed the PBP process to determine the bioink composition and establish a relationship between the material performance and printability. Standard 2D and 3D models were established to evaluate the printing results. Common biomedical models were divided into five structural types to facilitate practical applications, and the printing strategies of the structure were determined. GelMA based bioink was investigated, and excellent results were obtained. We did not focus on other types of materials, i.e., hyaluronic acid (HA) or alginate.

PBP is an interdisciplinary technology that involves optics, material properties, photo-crosslinking reaction kinetics, and engineering parameters. This study on printability based on engineering science has some limitations. Improving the optical precision requires high-precision printing equipment, which was not discussed in this paper. The improvement of the bioink characteristics is crucial to increase the printing success rate and printing accuracy. Existing bioink is mostly for special functions (mechanical toughness, excellent biological performance, etc.). Very few studies focused on printing performance optimization because there are few printing materials and a lack of guidance for the optimization requirements. The bioink requirements discussed in this paper focused only on improving the printing precision. The requirements for cell-laden printing and drug-carrying bioinks require further study.

Two standard models for evaluating the printing accuracy were proposed in this work. These models can be used to evaluate the printing feasibility of new materials and determine the range of the printing parameters. However, specific analysis and optimization are still needed for the precise printing of concrete structures. Moreover, five basic model structures were proposed, and the parameter selection for the GelMA bioink was given. Although the parameter values depend on the type of bioink, the analysis of the structural characteristics can be used for other applications. The printability analysis conducted in this study has limitations but it provides a framework for future research, with suggestions for specific topics that require analysis.

7. Conclusion

In this study, we summarized the printing strategies of PBP for fabricating various types of structures using GelMA hydrogel with high fidelity, high precision, and adjustable size. The material requirements for PBP were deduced by analyzing the printing process. The limitations of the GelMA hydrogel material system were summarized by investigating the photo-crosslinking reactions, highlighting the printing difficulties of PBP using soft GelMA hydrogels. The influences of the printing parameters and the GelMA and tartrazine concentrations were systematically investigated to increase the printing precision for practical applications. Five printing strategies were proposed for five basic structures commonly used in biomedical applications. The printing strategies were verified by printing custom-designed porous scaffolds using a pure GelMA hydrogel; the products exhibited high accuracy and good shape retention. Finally, the biocompatibility of the printed GelMA scaffolds was verified by seeding HUVECs on the surface of the printed structures. The HUVECs were well attached and spread uniformly on the outer and inner surfaces of the pores, demonstrating a high proliferation rate and excellent cell morphology. We believe that the proposed printing strategies for increasing the printability of GelMA hydrogels represent a practical method for fabricating custom hydrogel structures for tissue engineering and organ regeneration research. The PBP has significant potential for future biomedical applications for non-contact fabrication and the assessment of hypocoellular damage, especially with the continued development of hydrogel materials.

CRedit authorship contribution statement

Kang Yu: Conceptualization, Data curation, Formal analysis, Investigation, Writing – original draft, Methodology. **Xinjie Zhang:** Data curation, Investigation, Writing – original draft. **Yuan Sun:** Data curation, Formal analysis, Investigation, Methodology. **Qing Gao:** Conceptualization, Formal analysis. **Jianzhong Fu:** Conceptualization. **Xiujun Cai:** Funding acquisition, Writing – review & editing. **Yong He:** Conceptualization, Funding acquisition, Writing – review & editing.

Declaration of competing interest

We declare that we have no financial and personal relationships with other people or organizations that can inappropriately influence our work, there is no professional or other personal interest of any nature or kind in any product, service and/or company that could be construed as influencing the position presented in, the manuscript entitled, “Printability of Projection-based 3D Bioprinting”.

Acknowledgments

General: The authors acknowledge the Testing Center at the Suzhou Intelligent Manufacturing Research Institute for assistance with scanning electron microscopy and confocal microscopy.

Appendix A. Supplementary data

Supplementary data to this article can be found online at <https://doi.org/10.1016/j.bioactmat.2021.09.021>.

Funding

This study was sponsored by the National Key Research and Development Program of China (2018YFA0703000), the National Natural Science Foundation of China of China (No. U1909218), and the Science Fund for Creative Research Groups of the National Natural Science Foundation of China (No. T2121004).

References

- [1] S.V. Murphy, A. Atala, 3D bioprinting of tissues and organs, *Nat. Biotechnol.* 32 (8) (2014) 773–785.
- [2] C. Mandrycky, Z. Wang, K. Kim, D.H. Kim, 3D bioprinting for engineering complex tissues, *Biotechnol. Adv.* 34 (4) (2016) 422–434.
- [3] W. Cheng, J. Zhang, J. Liu, Z. Yu, Granular hydrogels for 3D bioprinting applications, *View* 1 (3) (2020).
- [4] K.H. Benam, S. Dauth, B. Hassell, A. Herland, A. Jain, K.J. Jang, K. Karalis, H. J. Kim, L. MacQueen, R. Mahmoodian, S. Musah, Y.S. Torisawa, A.D. van der Meer, R. Villenave, M. Yadid, K.K. Parker, D.E. Ingber, Engineered in vitro disease models, *Annu. Rev. Pathol.* 10 (2015) 195–262.
- [5] D. Dutta, I. Heo, H. Clevers, Disease modeling in stem cell-derived 3D organoid systems, *Trends Mol. Med.* 23 (5) (2017) 393–410.
- [6] S. Samavedi, N. Joy, 3D printing for the development of in vitro cancer models, *Current Opinion in Biomedical Engineering* 2 (2017) 35–42.
- [7] W. Peng, P. Datta, B. Ayan, V. Ozbolat, D. Sosnoski, I.T. Ozbolat, 3D bioprinting for drug discovery and development in pharmaceuticals, *Acta Biomater.* 57 (2017) 26–46.
- [8] M. Thomas, S.M. Willerth, 3-D bioprinting of neural tissue for applications in cell therapy and drug screening, *Front Bioeng Biotechnol* 5 (2017) 69.
- [9] N.G. Solanki, M. Tahsin, A.V. Shah, A.T.M. Serajuddin, Formulation of 3D printed tablet for rapid drug release by fused deposition modeling: screening polymers for drug release, drug-polymer miscibility and printability, *J. Pharmaceut. Sci.* 107 (1) (2018) 390–401.
- [10] M. Xie, Q. Gao, J. Fu, Z. Chen, Y. He, Bioprinting of novel 3D tumor array chip for drug screening, *Bio-Design and Manufacturing* 3 (3) (2020) 175–188.
- [11] S.W. Kim, H.J. Shin, C.S. Kay, S.H. Son, A customized bolus produced using a 3-dimensional printer for radiotherapy, *PLoS One* 9 (10) (2014), e110746.
- [12] H. Ma, J. Luo, Z. Sun, L. Xia, M. Shi, M. Liu, J. Chang, C. Wu, 3D printing of biomaterials with mussel-inspired nanostructures for tumor therapy and tissue regeneration, *Biomaterials* 111 (2016) 138–148.
- [13] E. George, P. Liacouras, F.J. Rybicki, D. Mitsouras, Measuring and establishing the accuracy and reproducibility of 3D printed medical models, *Radiographics* 37 (5) (2017) 1424–1450.

- [14] A. Isaacson, S. Swioklo, C.J. Connon, 3D bioprinting of a corneal stroma equivalent, *Exp. Eye Res.* 173 (2018) 188–193.
- [15] Q. Yan, H. Dong, J. Su, J. Han, B. Song, Q. Wei, Y. Shi, A review of 3D printing technology for medical applications, *Engineering* 4 (5) (2018) 729–742.
- [16] F. Kotz, K. Arnold, W. Bauer, D. Schild, N. Keller, K. Sachsenheimer, T.M. Nargang, C. Richter, D. Helmer, B.E. Rapp, Three-dimensional printing of transparent fused silica glass, *Nature* 544 (7650) (2017) 337–339.
- [17] L. Chen, Q. Wu, G. Wei, R. Liu, Z. Li, Highly stable thiol–ene systems: from their structure–property relationship to DLP 3D printing, *J. Mater. Chem. C* 6 (43) (2018) 11561–11568.
- [18] G. Varghese, M. Moral, M. Castro-García, J.J. López-López, J.R. Marín-Rueda, V. Yagüe-Alcaraz, L. Hernández-Afonso, J.C. Ruiz-Morales, J. Canales-Vázquez, Fabrication and characterisation of ceramics via low-cost DLP 3D printing, *Bol. Soc. Espanola Ceram. Vidr.* 57 (1) (2018) 9–18.
- [19] T.S.P. Grandhi, N. Zaman, A. Banda, V. Dhamankar, C. Chu, E. Perotta, I. Kadiyala, Mechanical Characterization of Extracellular Matrix Hydrogels Comparison of Properties Measured by Rheometer and Texture, 2018.
- [20] M.W. Tibbitt, K.S. Anseth, Hydrogels as extracellular matrix mimics for 3D cell culture, *Biotechnol. Bioeng.* 103 (4) (2009) 655–663.
- [21] M.T. Wolf, K.A. Daly, E.P. Brennan-Pierce, S.A. Johnson, C.A. Carruthers, A. D'Amore, S.P. Nagarkar, S.S. Velankar, S.F. Badylak, A hydrogel derived from decellularized dermal extracellular matrix, *Biomaterials* 33 (29) (2012) 7028–7038.
- [22] Christian Mandrycky, Zongjie Wang, Keekyoung Kim, Deok-Ho Kim, 3D bioprinting for engineering complex tissues, *Biotechnol. Adv.* 34 (4) (2016) 422–434.
- [23] Y. He, F. Yang, H. Zhao, Q. Gao, B. Xia, J. Fu, Research on the printability of hydrogels in 3D bioprinting, *Sci. Rep.* 6 (2016) 29977.
- [24] W. Jia, P.S. Gungor-Ozkerim, Y.S. Zhang, K. Yue, K. Zhu, W. Liu, Q. Pi, B. Byambaa, M.R. Dokmeci, S.R. Shin, A. Khademhosseini, Direct 3D bioprinting of perfusable vascular constructs using a blend bioink, *Biomaterials* 106 (2016) 58–68.
- [25] J. Yin, D. Zhao, J. Liu, Trends on physical understanding of bioink printability, *Bio-Design and Manufacturing* 2 (1) (2019) 50–54.
- [26] N. Faramarzi, I.K. Yazdi, M. Nabavinia, A. Gemma, A. Fanelli, A. Caizzone, L. M. Ptaszek, I. Sinha, A. Khademhosseini, J.N. Ruskin, A. Tamayol, Patient-specific bioinks for 3D bioprinting of tissue engineering scaffolds, *Adv Healthc Mater* 7 (11) (2018), e1701347.
- [27] G. Irmak, M. Gümüşderelioglu, Photo-activated platelet-rich plasma (PRP)-based patient-specific bio-ink for cartilage tissue engineering, *Biomed. Mater.* 15 (6) (2020).
- [28] Piyush Gupta, Kavita Vermani, Sanjay Garg, Hydrogels: from controlled release to pH-responsive drug delivery, *Drug Discov. Today* 7 (10) (2002) 569–579.
- [29] D. Tada, T. Tanabe, A. Tachibana, K. Yamauchi, Drug release from hydrogel containing albumin as crosslinker, *J. Biosci. Bioeng.* 100 (5) (2005) 551–555.
- [30] A. Blaeser, D.F. Duarte Campos, H. Fischer, 3D bioprinting of cell-laden hydrogels for advanced tissue engineering, *Current Opinion in Biomedical Engineering* 2 (2017) 58–66.
- [31] J. Park, S.J. Lee, S. Chung, J.H. Lee, W.D. Kim, J.Y. Lee, S.A. Park, Cell-laden 3D bioprinting hydrogel matrix depending on different compositions for soft tissue engineering: characterization and evaluation, *Mater Sci Eng C Mater Biol Appl* 71 (2017) 678–684.
- [32] J. Yang, Y.S. Zhang, K. Yue, A. Khademhosseini, Cell-laden hydrogels for osteochondral and cartilage tissue engineering, *Acta Biomater.* 57 (2017) 1–25.
- [33] A. Negro, T. Cherbuin, M.P. Lutolf, 3D inkjet printing of complex, cell-laden hydrogel structures, *Sci. Rep.* 8 (1) (2018) 17099.
- [34] S. Maharjan, D. Bonilla, P. Sindurakar, H. Li, W. Li, S. Duarte, A. Zarrinpar, Y. S. Zhang, 3D human nonalcoholic hepatic steatosis and fibrosis models, *Bio-Design and Manufacturing* 4 (2) (2021) 157–170.
- [35] T. Agarwal, N. Celikkan, M. Costantini, T.K. Maiti, P. Makvandi, Recent Advances in Chemically Defined and Tunable Hydrogel Platforms for Organoid Culture, *Bio-Design and Manufacturing*, 2021.
- [36] J. Christmann, C. Ley, X. Allonas, A. Ibrahim, C. Croutxé-Barghorn, Experimental and theoretical investigations of free radical photopolymerization: inhibition and termination reactions, *Polymer* 160 (2019) 254–264.
- [37] J.P. Fouassier, X. Allonas, D. Burget, Photopolymerization reactions under visible lights: principle, mechanisms and examples of applications, *Prog. Org. Coating* 47 (1) (2003) 16–36.
- [38] T.T.H. Luu, Z. Jia, A. Kanaev, L. Mauseur, Effect of light intensity on the free-radical photopolymerization kinetics of 2-hydroxyethyl methacrylate: experiments and simulations, *J. Phys. Chem. B* 124 (31) (2020) 6857–6866.
- [39] S. You, P. Wang, J. Schimelman, H.H. Hwang, S. Chen, High-fidelity 3D printing using flashing photopolymerization, *Addit Manuf* 30 (2019).
- [40] F.R. Schwarzl, Numerical calculation of storage and loss modulus from stress relaxation data for linear viscoelastic materials, *Rheol. Acta* 10 (2) (1971).
- [41] A. Marcilla, J.C. García, Rheological study of PVC plastisols during gelation and fusion, *Eur. Polym. J.* 33 (3) (1997) 349–355.
- [42] Y. Li, H. He, Y. Ma, Y. Geng, J. Tan, Rheological and mechanical properties of ultrahigh molecular weight polyethylene/high density polyethylene/polyethylene glycol blends, *Advanced Industrial and Engineering Polymer Research* 2 (1) (2019) 51–60.
- [43] Y. Li, Q. Mao, X. Li, J. Yin, Y. Wang, J. Fu, Y. Huang, High-fidelity and high-efficiency additive manufacturing using tunable pre-curing digital light processing, *Additive Manufacturing* 30 (2019).
- [44] Y. Sun, K. Yu, J. Nie, M. Sun, J. Fu, H. Wang, Y. He, Modeling the Printability of Photocuring and Strength Adjustable Hydrogel Bioink during Projection-Based 3D Bioprinting, *Biofabrication*, 2020.
- [45] Y. Li, Q. Mao, J. Yin, Y. Wang, J. Fu, Y. Huang, Theoretical prediction and experimental validation of the digital light processing (DLP) working curve for photocurable materials, *Additive Manufacturing* 37 (2021).
- [46] Y. Ma, N. Sun, R. Zhang, L. Guo, Y. She, J. Zheng, Z. Ye, Integrated color filter and polarizer based on two-dimensional superimposed nanowire arrays, *J. Appl. Phys.* 116 (4) (2014).
- [47] F. Steudel, T. Lisek, P.W. Nolte, U. Hofmann, T. von Wantoch, F. Lofink, S. Schweizer, Pixelated phosphors for high-resolution and high-contrast white light sources, *Opt Express* 26 (20) (2018) 26134–26144.
- [48] A. Seeboth, D. Löttsch, E. Potechius, Phase transitions and phase separations in aqueous polyether systems, *Colloid Polym. Sci.* 279 (2001) 696–704.
- [49] J.-C. Auger, R.G. Barrera, B. Stout, Scattering efficiency of clusters composed by aggregated spheres, *J. Quant. Spectrosc. Radiat. Transf.* 79–80 (2003) 521–531.
- [50] Wei Long Ng, et al., Vat polymerization-based bioprinting—process, materials, applications and regulatory challenges, *Biofabrication* 12 (2) (2020), 022001.
- [51] Wanlu Li, et al., Recent advances in formulating and processing biomaterial inks for vat polymerization-based 3D printing, *Advanced Healthcare Materials* 9 (15) (2020) 2000156.